
REAL-TIME BRAIN BIOMECHANICS PREDICTION WITH NEURAL OPERATORS: TOWARD CLINICALLY DEPLOYABLE TRAUMATIC BRAIN INJURY MODELS

Anusha Agarwal

Thomas Jefferson High School for Science and Technology
Alexandria, 6560 Braddock Rd
VA 22312, United States
2026aagarwal@tjhsst.edu

Dibakar Roy Sarkar

Johns Hopkins Whiting School of Engineering
Baltimore, 3400 N Charles St
MD 21218, United States
droysar1@jh.edu

Johns Hopkins Whiting School of Engineering
Baltimore, 3400 N Charles St
MD 21218, United States
aagarw57@jh.edu

Somdatta Goswami*

Johns Hopkins Whiting School of Engineering
Baltimore, 3400 N Charles St
MD 21218, United States
somdatta@jhu.edu

October 7, 2025

ABSTRACT

Background: Traumatic brain injury (TBI) remains a major public health concern, with over 69 million cases annually worldwide. Finite element (FE) models offer high-fidelity predictions of brain deformation but are computationally expensive, requiring hours per simulation and limiting their clinical utility for rapid decision-making.

Objective: This study benchmarks state-of-the-art neural operator (NO) architectures for rapid, patient-specific prediction of brain displacement fields, aiming to enable real-time TBI modeling in clinical and translational settings.

Methods: We formulated TBI modeling as an operator learning problem, mapping subject-specific anatomical MRI, magnetic resonance elastography (MRE) stiffness maps, and demographic features to full-field 3D brain displacement predictions. Four architectures - Fourier Neural Operator (FNO), Factorized FNO (F-FNO), Multi-Grid FNO (MG-FNO), and Deep Operator Network (DeepONet) were trained and evaluated on 249 MRE datasets across physiologically relevant frequencies (20 - 90 Hz).

Results: MG-FNO achieved the highest accuracy (MSE = 0.0023, 94.3% spatial fidelity) and preserved fine-scale features, while F-FNO converged 2 \times faster than standard FNO. DeepONet offered the fastest inference (14.5 iterations/s) with a 7 \times computational speed-up over MG-FNO, suggesting utility for embedded or edge computing applications. All NOs reduced computation time from hours to milliseconds without sacrificing anatomical realism.

Conclusion: NOs provide an efficient, resolution-invariant approach for predicting brain deformation, opening the door to real-time, patient-specific TBI risk assessment, clinical triage support, and optimization of protective equipment. These results highlight the potential for NO-based digital

*Corresponding author: somdatta@jhu.edu

twins of the human brain, enabling scalable, on-demand biomechanical modeling in both clinical and population health contexts.

Keywords: Neural operators, Fourier Neural Operator (FNO), Traumatic brain injury, Brain biomechanics, Magnetic Resonance Elastography (MRE), Deep learning, Real-time prediction, Digital twins, Protective equipment design

1 Introduction

Traumatic brain injury (TBI) is one of the leading causes of death and disability worldwide, affecting nearly 69 million people annually and contributing to significant long-term cognitive, emotional, and physical impairments. In the United States alone, TBI accounts for over 214,000 hospitalizations and more than 200 deaths per day, with associated healthcare costs exceeding \$76 billion per year [1]. Importantly, TBI is not limited to acute events, up to half of patients with mild TBI or concussion experience persistent neurological deficits six months after injury. These realities underscore an urgent need for accurate, patient-specific tools that can quantify brain tissue deformation and guide clinical decision-making after head impacts [2].

Finite element (FE) models have emerged as the gold standard for characterizing brain biomechanics. When combined with high-resolution neuroimaging, anatomical T1-weighted MRI and magnetic resonance elastography (MRE) that non-invasively quantifies viscoelastic properties such as shear modulus, FE simulations can predict subject-specific brain responses under controlled loading and reproduce experimental deformation fields measured with tagged MRI [3, 4, 5]. However, these models are computationally demanding, often requiring hours of runtime per subject due to the need to solve large, nonlinear partial differential equations over high-resolution meshes. This computational burden limits their integration into time-sensitive settings such as emergency triage, sideline concussion assessment, or rapid evaluation of helmet designs. Consequently, FE modeling remains largely a research tool rather than a clinically deployable technology [6].

Recent advances in machine learning (ML) have spurred efforts to accelerate TBI modeling [7]. Conventional ML approaches, such as convolutional neural networks, have been used to predict injury outcomes or scalar metrics like peak strain from imaging or kinematic features. While effective for outcome classification, these models typically lack spatial resolution and cannot produce the full-field brain deformation maps required for detailed injury risk assessment. More recent deep learning methods have trained neural networks directly on large libraries of FE simulations to predict voxelwise strain fields, achieving high accuracy but requiring extensive simulation datasets and sometimes generalizing poorly outside the training domain.

Neural operators (NOs) offer a powerful alternative. Unlike standard neural networks that approximate pointwise functions, NOs learn mappings between entire function spaces, making them resolution-invariant and able to generalize across new inputs and discretizations. Architectures such as the Deep Operator Network (DeepONet) [8] and Fourier Neural Operator (FNO) [9] have demonstrated success in fluid dynamics, elasticity, and climate modeling, achieving orders-of-magnitude faster inference than numerical solvers while retaining high accuracy. By directly approximating the solution operator of the governing equations from labeled datasets, NOs are well-suited for modeling complex, nonlinear biomechanical responses in the brain. Despite their promise, neural operators have not been systematically evaluated for TBI biomechanics. Key questions remain regarding which operator architecture best captures the nonlinear mapping from patient-specific anatomy and material properties to full-field brain deformation, and how these models trade off between accuracy, inference speed, and generalization. Addressing these questions is critical for translating NOs from research to clinical practice.

In this study, we present the first systematic benchmark of neural operator frameworks for subject-specific brain deformation prediction. Using a multimodal neuroimaging dataset of 249 magnetic resonance elastography (MRE) experiments [10], we compare four state-of-the-art NO architectures, FNO, Factorized FNO (F-FNO), Multi-Grid FNO (MG-FNO), and DeepONet for their ability to predict three-dimensional brain displacement fields across physiologically relevant frequencies (20–90 Hz). Our goals are threefold: (1) to formulate patient-specific TBI modeling as an operator learning problem, (2) to quantify the accuracy and computational efficiency of each architecture, and (3) to identify the approaches best suited for real-time, clinically deployable TBI risk assessment and protective equipment design.

The rest of the paper is organized as follows. Section 2 describes the dataset used for the study. Section 3 provides an overview of the deep neural operator theory and the architectures used in this study. Here, we describe the formulation of FNO, F-FNO, MG-FNO and DeepONet highlighting the differences in their implementations. Section 4 presents the numerical results and comparison of the models in terms of approximation accuracy. Section 5 outlines the conclusions and future scope of our study.

2 Dataset

The present study leverages recently developed, spatially resolved neuroimaging datasets that capture the biomechanics of the living human brain under controlled loading conditions [10]. These datasets provide three-dimensional, time-resolved displacement and strain fields, along with complementary anatomical and microstructural information, to enable subject-specific modeling and evaluation of computational traumatic brain injury (TBI) models. Data acquisition, as reported in [10], was conducted across three research sites - Washington University in St. Louis (WUSTL), the University of Delaware (UD) and the National Institutes of Health (NIH), with protocols tailored to different aspects of brain biomechanics.

2.1 Dataset Composition

The complete dataset includes multimodal imaging data from 300 participants (approximately 100 per site), encompassing a broad age range (14–80 years) and balanced sex representation. Participants were healthy volunteers recruited to capture normative biomechanical variability across age and sex. Each subject underwent one of three primary biomechanical imaging protocols, depending on site:

- Tagged MRI (NIH): Full-brain, time-resolved deformation fields were captured during impulsive, sub-injury rotational loading, with 18 ms temporal resolution and comprehensive brain coverage. These data provide a direct measure of dynamic tissue displacement under controlled acceleration, enabling validation of computational models.
- Magnetic Resonance Elastography (WUSTL): Brain displacement and strain fields were measured in response to harmonic skull motion across multiple excitation frequencies (20–90 Hz) with 3 mm isotropic voxel resolution. This modality captures frequency-dependent dynamic behavior and wave propagation patterns within brain tissue.
- High-Resolution MRE (UD): Spatially resolved maps of brain tissue viscoelastic properties—including complex shear modulus, stiffness, and damping ratio—were acquired at multiple frequencies (30–70 Hz) with 1.5 mm isotropic voxel resolution. These high-resolution data allow for subject-specific material property assignment in computational models.

All participants additionally underwent anatomical (T1- and T2-weighted) and diffusion-weighted MRI to provide structural context. These scans enable tissue segmentation, white matter tractography, and vascular feature extraction. Participant demographics and anthropometrics—including age, sex, height, weight, and brain volume—are also included, facilitating stratified analyses and investigation of age- and sex-specific effects on brain biomechanics. Acquisition parameters, such as scan direction and vibration frequency, are provided: direction (anterior-posterior [AP] or left-right [LR]) indicates scan orientation, while vibration frequency (20–90 Hz) corresponds to the mechanical excitations used to generate MRE displacement fields.

The present study only uses the WUSTL dataset for MRE displacement prediction. This source provides comprehensive measurements of brain dynamics under mechanical loading. In this dataset, 52 subjects were studied across various vibration frequencies, leading to a final dataset size of 249 samples.

2.2 Data Characteristics

To ensure cross-site consistency, all acquisitions are performed on Siemens 3T scanners with site-specific head coils, and harmonization procedures are applied to minimize inter-scanner variability. Imaging protocols include:

- Tagged MRI displacement and strain fields derived using the harmonic phase finite element (HARP-FE) method.
- MRE displacement data preprocessed with rigid-body motion estimation and phase unwrapping to recover full-field displacement vectors.
- High-resolution MRE displacement data inverted via nonlinear finite element methods to estimate storage and loss moduli (G' , G''), stiffness (μ), and damping ratio (ξ).

Derived outputs include full 3D displacement vectors, strain tensors, frequency-dependent material property maps, and summary scalar metrics such as maximum principal strain (MPS) and octahedral shear strain (OSS). Anatomical and diffusion-weighted images are processed through skull-stripping, atlas-based segmentation, and diffusion tensor imaging (DTI) tractography to generate label maps and axonal orientation fields, supporting integration of structural features into computational models.

Representative examples of the dataset including the attributes utilized in this study are provided in Figure 1.

2.3 Data Access and Format

All datasets are publicly disseminated through the Brain Biomechanics Imaging Resources repository hosted on the Neuroimaging Tools and Resources Collaboratory (NITRC) at <https://www.nitrc.org/projects/bbir>. Shared data include raw and processed displacement fields, strain fields, viscoelastic property maps, head kinematics, and corresponding anatomical MRI. Data are provided in Neuroimaging Informatics Technology Initiative (NIFTI) format. Anatomical data are registered to the MNI-152 atlas space and resampled at 0.8 mm isotropic resolution to facilitate cross-subject comparisons. All datasets are de-identified, collected under IRB-approved protocols, and shared under the GNU GPL v3.0 license.

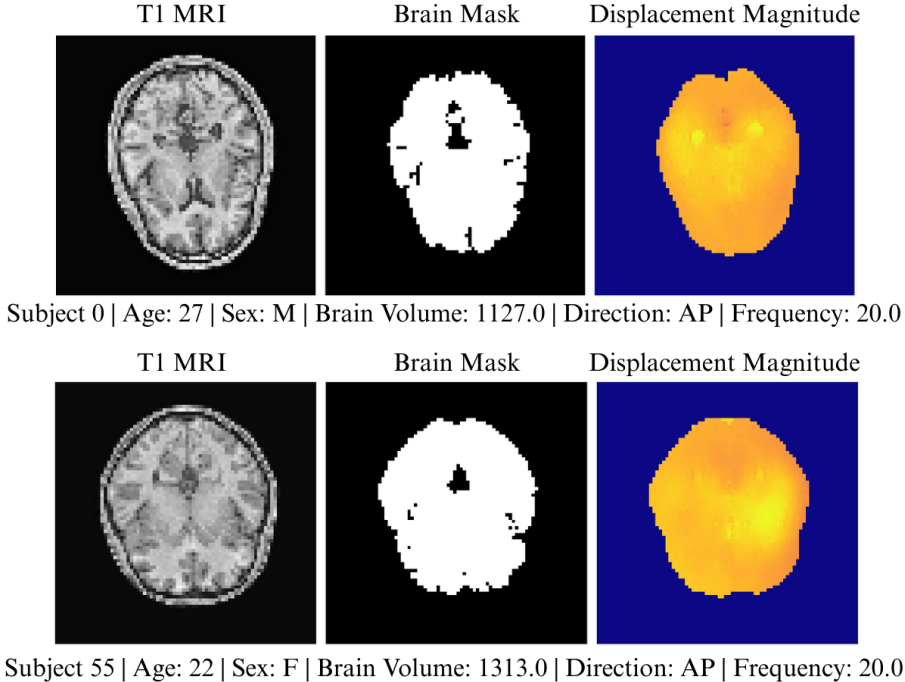


Figure 1: Representative visualization of the dataset, showing T1-weighted anatomical MRI (left), brain mask (middle), and displacement fields (right), along the central axial cross section for two samples. Displacement magnitude combines both the real and imaginary components of the displacement field. Direction relates to how the T1-weighted MRI was scanned and frequency relates to the rate at which mechanical vibrations are applied for MRE.

2.4 Data Processing

All data were stored in HDF5 format. We processed a total of 249 samples, partitioned into training, validation, and test subsets using a 70:10:20 stratified split, ensuring demographic balance across splits. We developed a custom PyTorch-compatible data loader to parse each HDF5 file, extracting both imaging and metadata into structured dictionaries. After parsing and preprocessing each sample, all relevant tensors and metadata were stored in a list of Python dictionaries, with each dictionary representing a complete training sample. This structure allows flexible access during batching, data augmentation, and multimodal model construction. Each dictionary contains all fields (T1 volume, displacement field, brain mask, and metadata) for a single subject. These were cached in memory for rapid batching and I/O-efficient training.

2.4.1 Data Scaling

To ensure numerical stability and accelerate convergence during training, we applied a series of normalization steps to both imaging and demographic data. Scaling was performed globally across the entire dataset where applicable, using min-max normalization schemes tailored to each data modality.

T1-weighted MRI volumes were normalized on a per-voxel basis using global minimum and maximum intensity values computed across all subjects. This strategy preserves spatial contrast patterns between individuals while bringing voxel values into the $[0, 1]$ range. For each voxel coordinate (x, y, z) , we computed:

$$\text{voxel}_{\min}(x, y, z) = \min_i \text{T1}_i(x, y, z), \quad \text{voxel}_{\max}(x, y, z) = \max_i \text{T1}_i(x, y, z)$$

where i indexes subjects. The final T1 volumes were scaled as:

$$\text{T1}_{\text{scaled}} = \frac{\text{T1} - \text{voxel}_{\min}}{\text{voxel}_{\max} - \text{voxel}_{\min}}$$

Displacement fields were globally scaled using the minimum and maximum of all displacement magnitudes across the dataset. This preserves relative deformation strength while ensuring that all values lie in the unit interval. Scalar demographic features (age and brain volume) were normalized using dataset-wide minimum and maximum values. Age was linearly scaled to $[0, 1]$ using standard min-max scaling:

$$\text{Age}_{\text{scaled}} = \frac{\text{Age} - \text{Age}_{\min}}{\text{Age}_{\max} - \text{Age}_{\min}}$$

Brain volume, on the other hand, was scaled to the range $[0.1, 0.9]$ to preserve margin for potential out-of-distribution values. Invalid or missing demographic entries (e.g., age ≤ 0) were encoded with a sentinel value of -1 and excluded from model input where appropriate.

Brain Masking. To restrict the analysis to anatomically relevant regions, we applied a binary mask that delineates brain tissue from the surrounding background. The mask assigns a value of 1 to voxels corresponding to brain tissue and 0 to non-brain regions, thereby excluding non-brain voxels from subsequent computation. Importantly, the mask does not remove noise directly; rather, it isolates the spatial extent of the brain so that preprocessing and model training are performed only within this region. Masking was applied prior to scaling to prevent artificial amplification of background values and to reduce unnecessary computation outside the brain. This ensures that normalization and intensity scaling are applied exclusively to meaningful brain voxels, improving training stability and reconstruction quality. It is important to note that the brain masks are provided in the dataset, and we utilize these pre-existing masks to constrain the learning process to anatomically relevant regions.

3 Deep Neural Operators

Neural operators (NOs) are a class of deep learning architectures that learn mappings between infinite-dimensional function spaces, offering a powerful alternative to traditional physics-based solvers. Rather than approximating pointwise functions, NOs learn the solution operator of a physical system, mapping input fields such as material properties or boundary conditions directly to output fields such as displacements. Critically, NOs are resolution-invariant and generalize across discretizations, enabling efficient surrogate modeling of complex PDE systems. They have shown state-of-the-art performance in fluid dynamics, elasticity, and other domains where long-range spatial dependencies and high-dimensional fields are essential.

The first NO architecture, the Deep Operator Network (DeepONet), was introduced in 2019 [8], building on the universal approximation theorem for operators by Chen & Chen [11]. DeepONet employs a dual-network structure: a branch network encodes input functions sampled at sensor points, while a trunk network encodes spatial or spatio-temporal output coordinates. Their inner-product fusion enables accurate and efficient surrogate modeling, and DeepONet has since been applied to a range of high-dimensional scientific problems.

Another major class of NOs uses spectral integral formulations. The Fourier Neural Operator (FNO) parameterizes convolution kernels in the Fourier domain, capturing global structures efficiently and achieving orders-of-magnitude faster inference than conventional solvers [9]. Building on this, the Factorized FNO (F-FNO) introduces separable spectral layers and improved residual connections, reducing parameter counts while allowing deeper networks [12]. The Multi-Grid Tensorized FNO (MG-FNO) further decomposes the input domain hierarchically and tensorizes Fourier kernels, enabling high-resolution simulations with fewer weights [13]. These architectures provide complementary advantages, improved representation power, parameter efficiency, and scalability, making them well-suited for capturing heterogeneous, high-resolution brain deformations.

NOs have been successfully applied across diverse domains, including materials modeling [14, 15], earthquake response prediction [16], weather forecasting [17], fluid dynamics [18], and biomedical imaging [19]. They have enabled breakthroughs in solving differential equations [20], accelerated real-time prediction of complex dynamics [21, 22], and coupled seamlessly with numerical solvers for hybrid approaches [23]. Applications also include inverse problems

and parameter estimation in heterogeneous systems [24, 25], time-dependent PDE modeling via physics-informed temporal operators [26, 27], and resolution-independent formulations that maintain accuracy across discretizations [28]. Recent advances include separable physics-informed architectures that break the curse of dimensionality [29], synergistic multitask frameworks for efficient PDE solution [30], and stochastic modeling of structural systems under natural hazards [16].

In this work, we focus on benchmarking four state-of-the-art NO architectures: FNO [9], F-FNO [12], MG-FNO [13], and DeepONet [8] for patient-specific TBI modeling. All models were implemented in PyTorch [31], and we detail their architecture, training strategies, and hyperparameter optimization in the following sections.

3.1 Fourier Neural Operator

Data Representation. After T1 and scalar data have been preprocessed, scalar data must be projected onto a 3D grid to allow the model to access all scalar features at every single voxel in the T1 image grid. Age, brain volume, sex, frequency, and direction are the 5 selected scalar features for input. These features are then projected onto a field of the same depth, height, and width as the input of the T1 image so that each feature is in shape [1, W, H, D]. From here, all features are stacked along the first input channel, creating an input of size [6, W, H, D]. A key design decision was to project scalar metadata into dense 3D fields instead of concatenating them at later layers in the network. While both approaches are valid, projection at the input stage enforces spatial conditioning, ensuring that metadata influences the model uniformly across the entire volume from the very beginning of training. This allows the network to learn interactions between global metadata and local structural features in the T1 image, rather than deferring this integration until later layers, where spatial correspondence might already be abstracted away. In practice, this strategy encourages the model to treat scalar features as fundamental contextual priors, directly modulating voxel-level representations.

Positional Encoding. As FNO learns in a 3D spatial domain, adding positional features enhances the model’s ability to reason in a location-informed grid rather than relying solely on appearance features. To encode spatial position, we generate continuous positional grids across the x, y, and z dimensions using the PyTorch `linspace` function. Each grid spans the normalized range [0, 1], where 0 represents one boundary of the axis and 1 represents the opposite boundary. This normalization ensures scale invariance, making the encoding independent of the absolute image dimensions and instead tied to relative voxel location. Each positional grid is appended along the first channel of the existing input, allowing the model to distinguish between structurally similar but spatially distinct features (e.g., left vs. right hemispheres). With this addition, the final input for FNO prediction takes the shape [9, W, H, D], consisting of the original six scalar/T1 channels and three positional channels.

3.1.1 FNO Architecture

We employ the Fourier Neural Operator (FNO), which leverages spectral convolution layers to capture long-range spatial dependencies. Below we outline the specific architecture used in our study, which operates as follows:

Lifting Layer:

The input function $u(x)$, discretized on a uniform grid, is first lifted to a higher-dimensional representation using a pointwise (fully connected) linear layer:

$$v_0(x) = P(u(x)), \quad \text{where } P : \mathbb{R}^d \rightarrow \mathbb{R}^m$$

This increases the feature dimension from the input space to a latent space suitable for learning complex operators.

Fourier Layers:

Each Fourier layer performs a global operation through the following steps:

- *Fourier Transform:* Convert the spatial representation $v_j(x)$ into the frequency domain using the fast Fourier transform (FFT):

$$\hat{v}_j(k) = \mathcal{F}[v_j](k)$$

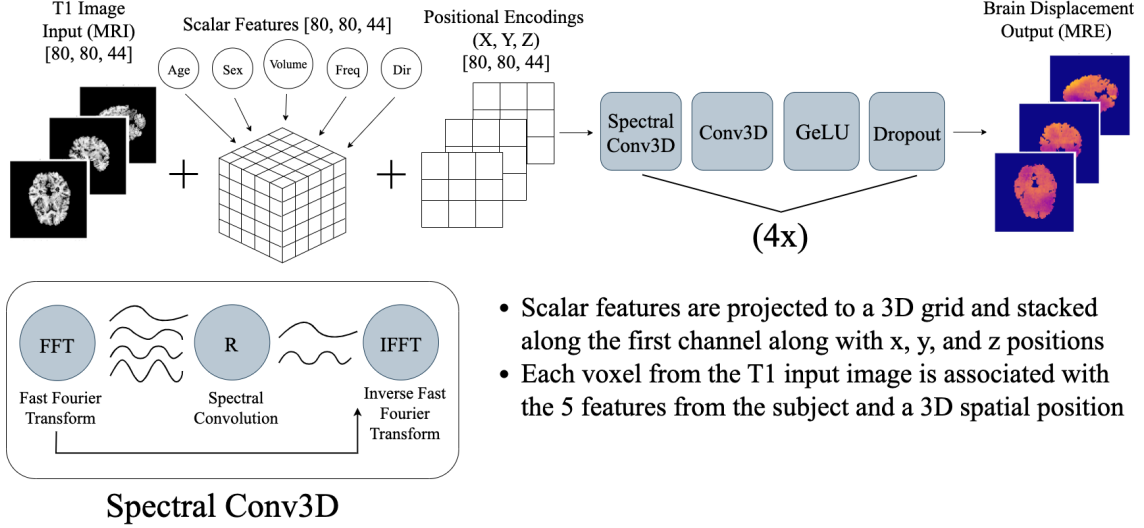
- *Spectral Convolution:* Apply a learned complex-valued linear transformation in the frequency domain:

$$\hat{v}_{j+1}(k) = W(k)\hat{v}_j(k)$$

Typically, only the lowest K Fourier modes are retained and updated, reducing computational cost and acting as a form of regularization.

- *Inverse Fourier Transform:* Transform the result back to the spatial domain:

$$v_{j+1}(x) = \mathcal{F}^{-1}[\hat{v}_{j+1}](x)$$



- Scalar features are projected to a 3D grid and stacked along the first channel along with x, y, and z positions
- Each voxel from the T1 input image is associated with the 5 features from the subject and a 3D spatial position

Spectral Conv3D

Figure 2: Fourier Neural Operator (FNO) Architecture for Brain Displacement Prediction. The network takes T1 MRI images [80, 80, 44] as primary input, which are augmented with scalar subject features (age, sex, volume, frequency, direction) and 3D positional encodings (X, Y, Z coordinates), all projected to matching grid dimensions [80, 80, 44]. These multi-modal inputs are concatenated along the channel dimension and processed through the core Spectral Conv3D operation, which performs convolution in the frequency domain via Fast Fourier Transform (FFT), spectral convolution (R), and Inverse FFT. The spectral convolution is followed by standard 3D convolution, GeLU activation, and dropout layers (repeated 4 times) to predict 3D brain displacement fields for Magnetic Resonance Elastography (MRE).

- *Nonlinearity:* Apply a non-linear activation function (in this case, GELU [32]) pointwise in the spatial domain.

We repeat this process in four layers, enabling the model to learn complex nonlinear mappings in a globally coupled manner.

Projection Layer:

After the sequence of Fourier layers, a final pointwise linear layer maps the output from the latent space back to the desired output function space:

$$u_{\text{out}}(x) = Q(v_n(x)), \quad \text{where } Q : \mathbb{R}^m \rightarrow \mathbb{R}^d$$

The schematic of this architecture is presented in Figure 2.

3.1.2 Factorized Fourier Neural Operator (F-FNO).

We build upon the Factorized Fourier Neural Operator (F-FNO) architecture proposed by Tran et. al [12]. This model enhances the traditional FNO framework by factorizing the spectral convolution into one-dimensional operations along each spatial axis, reducing the number of learnable parameters and the computational cost by over two orders of magnitude while retaining accuracy.

Given an input tensor $u \in \mathbb{R}^{B \times C_{\text{in}} \times D \times H \times W}$, we first apply a lifting layer

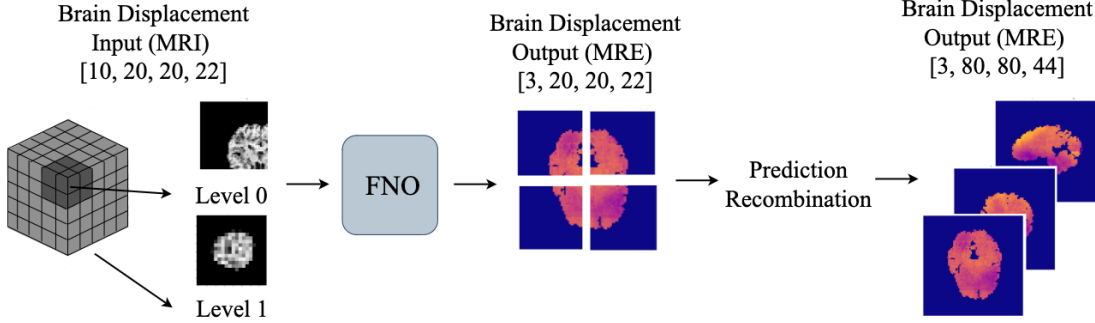
$$v_0 = \sigma(\text{Conv}_{1 \times 1}(u)), \quad v_0 \in \mathbb{R}^{B \times d_{\text{model}} \times D \times H \times W}, \quad (1)$$

where σ denotes the GELU activation and $d_{\text{model}} = 64$ is the latent channel dimension.

Each subsequent F-FNO layer applies three factorized spectral convolutions, one per spatial dimension, followed by pointwise mixing and a residual connection:

$$v_{\ell+1} = v_{\ell} + \sigma \left(W_2 \sigma \left(W_1 \mathcal{F}^{-1} \left(\sum_{j=1}^3 \mathcal{P}_j (\mathcal{F}_j(v_{\ell}) \cdot \Theta_j) \right) \right) \right), \quad (2)$$

where \mathcal{F}_j and \mathcal{F}^{-1} denote the forward and inverse one-dimensional Fourier transforms along dimension $j \in \{D, H, W\}$, Θ_j are complex-valued learnable weights truncated to the lowest m_j modes, and \mathcal{P}_j projects the truncated spectrum



- Input Space of $[80, 80, 44]$ divided into 32 subsections of size $[20, 20, 22]$
- Full domain is downsampled into $[20, 20, 22]$ blocks and added as an input channel
- Each patch is processed independently and recombined after prediction

Figure 3: Multi-Grid Fourier Neural Operator (FNO) Architecture for Hierarchical Brain Displacement Prediction. The input domain $[80, 80, 44]$ is spatially decomposed into 32 non-overlapping subsections of size $[20, 20, 22]$ to enable multi-scale processing. The brain MRI data is processed at multiple resolution levels: Level 0 operates on downsampled blocks $[20, 20, 22]$, while Level 1 processes the full domain context. Each level is fed into separate FNO networks that independently predict 3-component displacement fields $[3, 20, 20, 22]$ for their respective scales. The multi-scale predictions are then recombined through a prediction recombination module to reconstruct the final high-resolution brain displacement output $[3, 80, 80, 44]$ for MRE analysis. This hierarchical approach allows the model to capture both local fine-grained deformation patterns within individual patches and global long-range dependencies across the entire brain domain, improving computational efficiency while maintaining prediction accuracy for biomechanical modeling.

back to the original resolution via zero-padding. The $1 \times 1 \times 1$ convolutions W_1 and W_2 serve as channel mixers, and σ is again the GELU nonlinearity. In our setting, we retain $m_1 = 40$, $m_2 = 40$, and $m_3 = 12$ modes respectively.

Stacking $L = 4$ such layers yields the encoded representation v_L , which is then mapped to the three-dimensional displacement field via a projection head:

$$\hat{u} = \text{Conv}_{1 \times 1}(\sigma(\text{Conv}_{1 \times 1}(v_L))), \quad \hat{u} \in \mathbb{R}^{B \times 3 \times D \times H \times W}. \quad (3)$$

This architecture preserves the global receptive field of the Fourier operator while substantially lowering memory usage and training cost. By truncating to low-frequency modes, the model also enforces smoothness and reduces aliasing artifacts, which is particularly beneficial for large-scale 3D scientific data.

3.1.3 Multi-Grid Fourier Neural Operator (MG-FNO).

To further improve scalability, spatial continuity, and localization, we integrated a multigrid approach into the FNO structure, inspired by the framework proposed by Kossaifi, et. al [13]. Rather than processing the entire 3D domain holistically, the MG-FNO partitions the input volume into smaller, non-overlapping subdomains (patches). Each patch is processed independently, enabling the network to learn localized deformation patterns with greater efficiency while still incorporating essential global context. In our implementation, the domain is divided into patches of size $[20, 20, 22]$, which evenly partition the T1-weighted MRI volumes of shape $[80, 80, 44]$. For each local patch, we additionally provide a downsampled global representation of the T1 input. This global context is generated by interpolating the full-resolution T1 channel to a coarser scale (factor of 4), and then resizing it back to match the patch dimensions. By concatenating this global T1 context with each local patch, the network maintains awareness of long-range dependencies and overall brain geometry, while still learning highly localized features. The resulting patch-level input has an augmented channel dimension ($[10, 20, 20, 22]$), compared to the baseline FNO input ($[9, 20, 20, 22]$). Once all patches are processed, predictions are reassembled into the full displacement field by directly mapping each patch back into its corresponding subdomain location. This patch-based reconstruction ensures consistency across the full domain while enabling fine-grained learning at the patch level. The architecture is visualized in Figure 3.

3.2 DeepONet Architecture

The Deep Operator Network (DeepONet) is a neural architecture designed to learn nonlinear operators that map between function spaces, making it particularly effective for modeling mappings from input functions (e.g., images) to output functions (e.g., deformation fields) [8].

DeepONet consists of two primary components: a *branch network* and a *trunk network*. The branch network encodes the input functions and associated scalar features, while the trunk network encodes the spatial coordinates where the output is evaluated. The final output is obtained via an inner-product fusion of branch and trunk features, enabling the model to decouple spatial and functional dependencies.

Branch Network. In our implementation, the branch network is composed of multiple subnetworks, each processing a specific modality or scalar feature:

- **CNN branch:** Processes the 2D slices of the T1-weighted MRI to extract high-level image features. The CNN consists of three convolutional layers with batch normalization and pooling (two max-pooling and one average pooling), followed by fully connected layers with dropout to produce a 300-dimensional embedding.
- **FNN branches:** Each scalar attribute, scan direction, vibration frequency, sex, brain volume, and age, is processed through a separate fully connected feedforward network (FNN), each producing a 300-dimensional embedding. These subnetworks capture the effect of acquisition parameters and participant-specific demographics on the predicted displacement.

The outputs of all branch subnetworks are combined multiplicatively to form a single 300-dimensional branch representation that encodes both anatomical and scalar information.

Trunk Network. The trunk network encodes the spatial coordinates of the voxels at which the displacement is to be predicted. In our implementation, the trunk network is a multilayer perceptron with linear layers and ReLU activations, mapping the 3D coordinates (x, y, z) to a feature vector of the same dimensionality as the branch output (300 dimensions).

Output Fusion. The final displacement prediction at each voxel is computed via an elementwise inner product between the branch embedding and the corresponding trunk embedding for each output dimension:

$$\mathbf{u}(x) \approx \sum_{i=1}^p b_i(u) \cdot t_i(x), \quad \mathbf{u}(x) = (u_x, u_y, u_z),$$

where $b_i(u)$ is the i -th branch feature and $t_i(x)$ is the i -th trunk feature. In our implementation, the branch output is split into three 100-dimensional vectors corresponding to the x , y , and z displacement components, which are fused with the corresponding trunk features via the inner product.

This design allows the DeepONet to efficiently learn complex mappings from multimodal brain imaging data and scalar features to full 3D displacement fields, while retaining flexibility to generalize across subjects and acquisition parameters. Architecture visualization is in Figure 4.

3.3 Model Training and Validation

The models were trained to predict the three displacement components as outputs, using the T1-weighted image and associated scalar features as inputs. Prior to training, displacement fields were scaled and masked to enforce stability, reduce numerical variance, and ensure that predictions were constrained to anatomically valid regions. This setup allowed the networks to directly learn the physical continuity and spatial structure of displacement without relying on intermediate transformations or surrogate targets.

All models were trained on the Rockfish cluster at Johns Hopkins University, specifically on the `ica100` partition. Each node in this partition is equipped with 64 CPU cores across 2 sockets, 256 GB of RAM, and 4 NVIDIA A100 GPUs, providing the computational power necessary for training large-scale operator learning models.

Training schedules were standardized across architectures: all Fourier Neural Operator (FNO) models were trained for 1000 epochs, with the exception of the Factorized FNO, which was able to converge in 500 epochs. The DeepONet model was trained with 5000 epochs. The loss history for each training run is reported in Figure 5., showing both the progression of training loss and validation loss. These curves highlight the comparative convergence behavior of the models and provide insight into generalization performance.

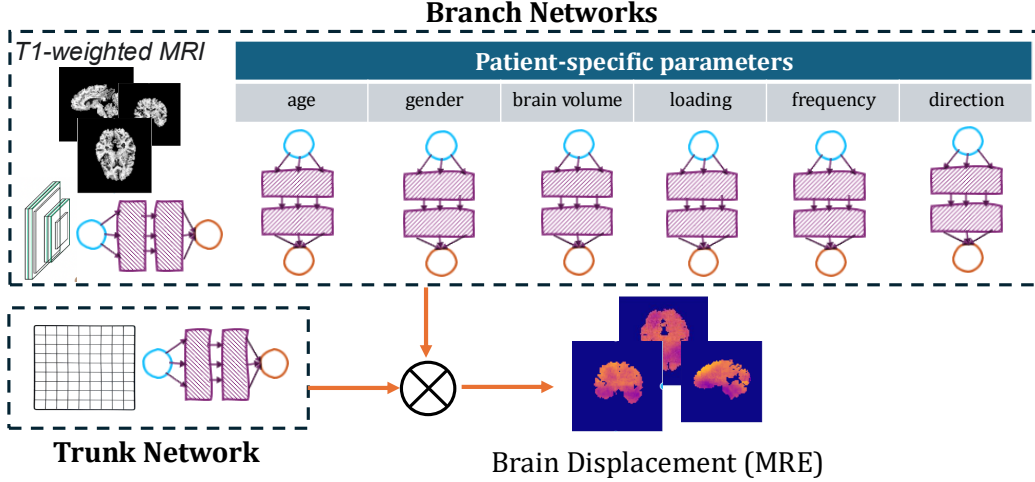


Figure 4: Deep Operator Network (DeepONet) Architecture for Brain Displacement Prediction. The architecture employs six branch networks and one trunk network to map multimodal inputs to 3D displacement fields. A CNN branch processes T1-weighted MRI slices $[80 \times 80 \times 44]$ through convolutional layers with batch normalization and pooling to extract 300D anatomical features, while five separate FNN branches encode scalar parameters (scan direction, vibration frequency, sex, brain volume, age) into 300D embeddings each. All branch outputs are fused via element-wise multiplication to create a unified 300D representation encoding both anatomical and demographic information. The trunk network processes 3D spatial coordinates (x, y, z) through multilayer perceptrons to generate 300D spatial basis functions at each voxel location. For displacement prediction, the 300D branch vector is partitioned into three 100D segments corresponding to x -, y -, and z -components, which undergo inner-product fusion with corresponding trunk segments via Einstein summation. This operator learning framework generates continuous 3D displacement fields $[\text{Batch} \times \text{N_voxels} \times 3]$ by decoupling spatial and functional dependencies, enabling prediction of brain tissue deformation from multimodal anatomical and acquisition parameters for MR elastography applications.

3.3.1 Hyperparameter Tuning

A learning rate of 1×10^{-3} was used throughout most of the training process, with the AdamW optimizer [33] ($\text{weight_decay} = 1 \times 10^{-5}$) to balance fast convergence with regularization. To further stabilize optimization, we employed a ReduceLROnPlateau scheduler, which adaptively decayed the learning rate by a factor of 0.5 if validation loss did not improve for 10 epochs.

Loss was computed using a masking voxel-wise Mean Squared Error (MSE) criterion such that gradients only accumulated within anatomically valid brain regions. Specifically, losses were first calculated per voxel and then multiplied by the binary brain mask before reduction, ensuring that boundary regions or background voxels did not bias the optimization process.

During each epoch, both training and validation losses were logged. The best-performing checkpoint (based on validation loss) was automatically saved to disk, allowing recovery of the optimal model state for inference.

Modes Selection. In Fourier Neural Operator (FNO) training, the primary tunable parameter is the number of Fourier modes retained in each spatial dimension (x, y, z) . For an input domain with size $N_x \times N_y \times N_z$, the maximum number of independent modes in each dimension is given by:

$$k_{\max}^x = \frac{N_x}{2} + 1, \quad k_{\max}^y = \frac{N_y}{2} + 1, \quad k_{\max}^z = \frac{N_z}{2} + 1.$$

Retaining fewer modes acts as a low-pass filter and helps prevent overfitting while reducing computational cost.

For both the standard FNO and the fully-factorized FNO (F-FNO), we found that using approximately half of the maximum available modes in each dimension provided the best performance, resulting in $[k_x, k_y, k_z] = [40, 40, 12]$. For the multi-grid FNO (MG-FNO), it was advantageous to use the full set of available modes, corresponding to $[k_x, k_y, k_z] = [20, 20, 12]$, to better capture high-frequency components conditioned on global inputs.

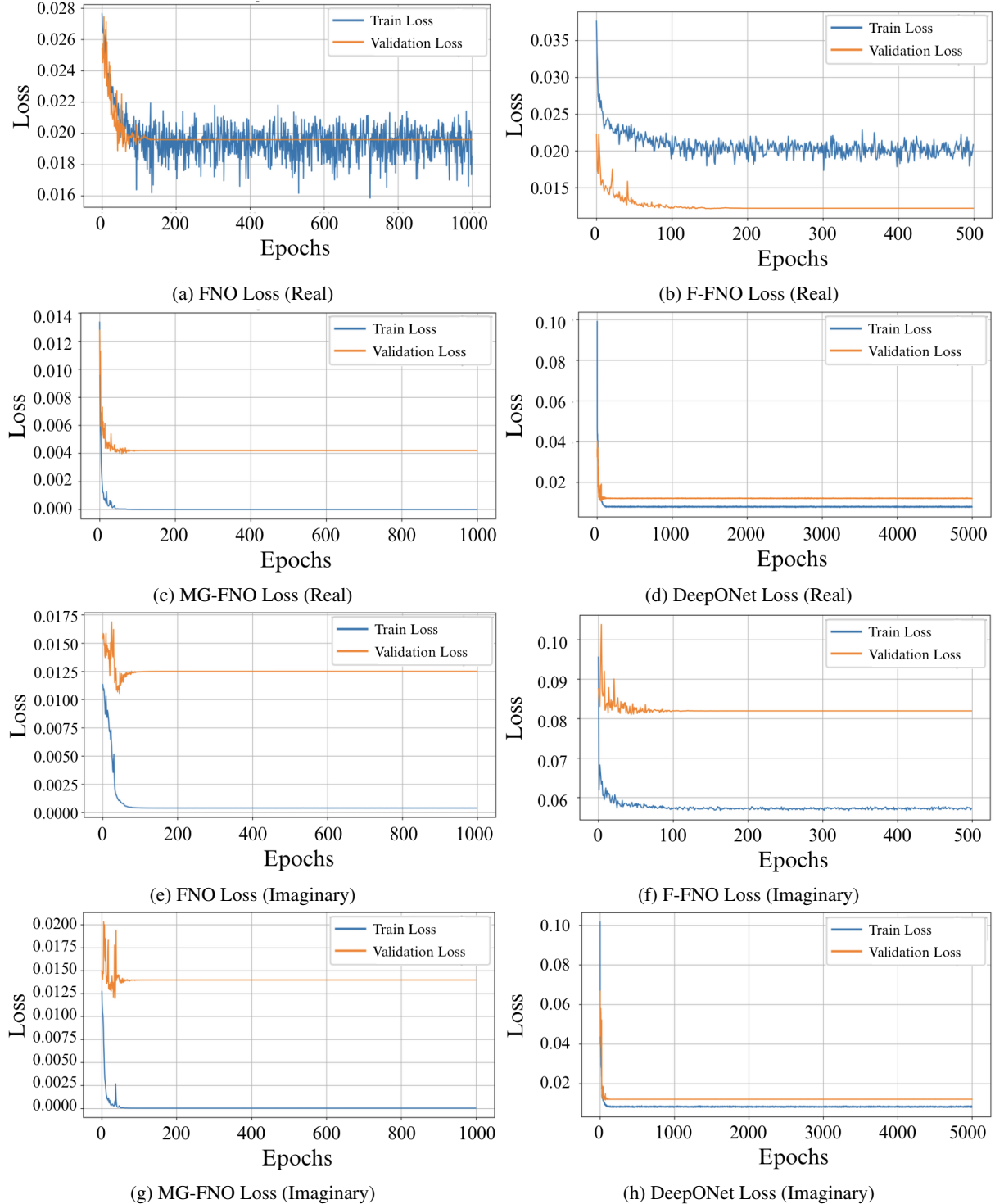


Figure 5: Training and Validation Losses across Models. Both the FNO and F-FNO were able to converge much faster on the imaginary displacement fields in comparison to the real displacement. In general, the F-FNO was able to converge in fewer epochs than the other FNO variants.

4 Results

We evaluated the performance of the benchmarked neural operator models using the *mean squared error* (MSE) metric, defined as

$$\text{MSE} = \frac{1}{N} \sum_{i=1}^N (y_i - \hat{y}_i)^2, \quad (4)$$

where N is the number of samples, y_i represents the ground-truth displacement or field value, and \hat{y}_i denotes the corresponding prediction from the model. MSE was chosen as the primary performance indicator because it penalizes large deviations more strongly than other error metrics, making it particularly sensitive to the sharp displacement gradients present in traumatic brain injury (TBI) simulations. For completeness, we also report mean absolute error (MAE), root mean squared error (RMSE), and accuracy.

The dataset comprises 249 samples, which were split into 174 samples for training, 25 for validation, and 50 for testing. This partitioning ensured that model performance was assessed on data not seen during training, enabling unbiased evaluation of generalization.

Table 1 reports the predictive performance of the models on real and imaginary displacement fields, while Table 2 summarizes computational efficiency in terms of iterations per second.

Table 1: Performance Comparison of Benchmarked Architectures on Real and Imaginary Displacement Fields. MSE is highlighted as the primary evaluation metric.

Direction	Model	MAE	MSE	RMSE	Accuracy
Real	Fourier Neural Operator	0.0352	0.0041	0.0640	0.9118
	Factorized FNO	0.0265	0.0025	0.0496	0.9385
	Multi-Grid FNO	0.0276	0.0023	0.0481	0.9429
	DeepONet	0.0567	0.0064	0.0801	0.8349
Imaginary	Fourier Neural Operator	0.0070	0.0430	0.2074	0.8901
	Factorized FNO	0.0525	0.0101	0.1005	0.8753
	Multi-Grid FNO	0.0375	0.0045	0.0674	0.9042
	DeepONet	0.0517	0.0068	0.0569	0.9200

Table 2: Compute Efficiency of Benchmarked Architectures. Higher iterations per second indicate faster inference.

Model	Iterations/Second	Parameters
Fourier Neural Operator	1.98	1415628838
Factorized FNO	1.44	6945574
Multi-Grid FNO	8.08	353945734
DeepONet	14.54	2087927

In the following subsections, we present results for each neural operator individually. Within each subsection, we discuss the performance of the vanilla operator and its variants in detail, highlighting comparative accuracy, error metrics, and architectural differences. A full comparison of each model’s predictions and errors is visualized in Fig. 7.

4.1 FNO and Variant Architectures Evaluation

The baseline FNO achieved an MSE of 0.0041 on real displacement fields, with corresponding MAE of 0.0352 and RMSE of 0.0640. Despite producing physically consistent predictions, the FNO tended to underpredict displacement magnitudes in high-gradient regions. These errors were spatially structured, manifesting as streaking artifacts aligned with grid axes (Fig. 6), reflecting a limitation of the Fourier representation in resolving anisotropic fine-scale features. Performance declined on imaginary displacement fields, where the MSE rose substantially to 0.0430, highlighting the difficulty of capturing abrupt transitions in magnitude. Computationally, the FNO processed approximately 1.98 iterations per second, representing moderate efficiency relative to its variants. These observations motivate the use of architectural modifications, such as factorization and global conditioning, to enhance the model’s ability to capture both high-frequency local features and long-range dependencies.

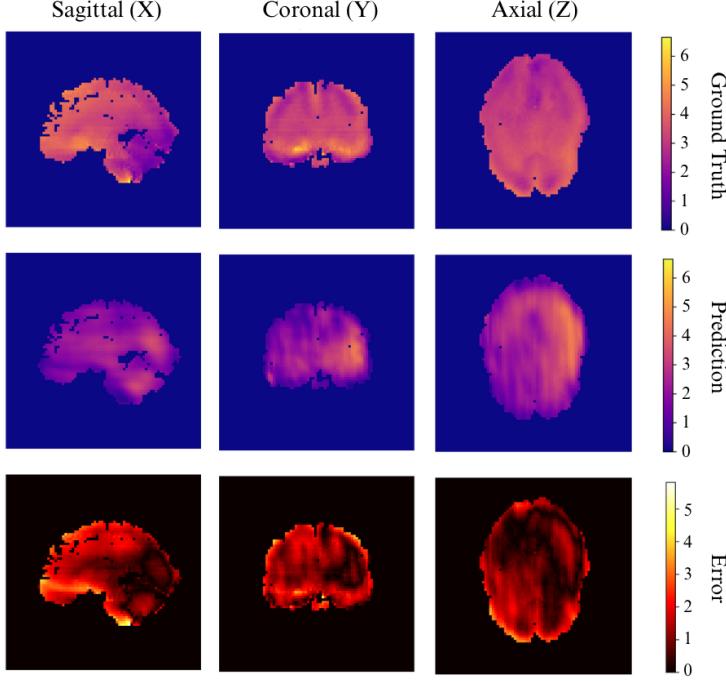


Figure 6: FNO Prediction Artifacts in Brain Displacement Fields. Orthogonal views showing ground truth (top), FNO predictions (middle), and prediction errors (bottom) across sagittal, coronal, and axial planes. The model exhibits characteristic axis-aligned streaking artifacts, most prominent in coronal and axial views, due to underprediction in high-gradient regions.

Factorized Fourier Neural Operator. The Factorized FNO (F-FNO) improved predictive accuracy on real displacement fields relative to the baseline, achieving an MSE of 0.0025 (a 39% reduction compared to the FNO) and accuracy of 0.9385. This improvement was achieved with a substantially more compact parameterization owing to low-rank factorization of the Fourier weight matrices. This allowed it to train and test much faster than the FNO, with approximately $203.8\times$ fewer parameters compared to the traditional FNO, yielding significantly lower memory consumption and faster inference while retaining predictive expressivity. Qualitatively, the F-FNO reduced streaking artifacts and produced smoother predictions, suggesting that the factorized representation improved the stability and smoothness of the learned operators. However, performance on imaginary displacement fields was inconsistent: the model yielded an MSE of 0.0101, better than the FNO baseline, but exhibited larger MAE (0.0525) and RMSE (0.1005), suggesting instability in capturing high-magnitude transitions. This persistence of underestimation bias in high-displacement regions indicates a limitation in the model’s ability to fully capture extreme variations, likely due to its more compact parameterization. The computational efficiency of the F-FNO was somewhat lower than the baseline (1.44 iterations per second), reflecting overhead introduced by factorization.

Multi-Grid Fourier Neural Operator. The MG-FNO achieved the strongest overall performance, with an MAE of 0.0276, RMSE of 0.0481, and accuracy of 0.9429. It achieves the lowest MSE on both real (0.0023) and imaginary (0.0045) components; relative reductions versus the baseline are $\approx 43.9\%$ (real) and $\approx 89.5\%$ (imag) respectively. Notably, the MG-FNO preserved finer-scale details and exhibited improved robustness in high-gradient regions, suggesting that its multiscale representation enhances recovery of both global and local displacement features. The improvement can be attributed to the multigrid architecture, which explicitly captures hierarchical frequency content and facilitates the exchange of information between coarse- and fine-resolution levels. This structure mitigates the tendency of standard FNOs to over-smooth sharp transitions, allowing the model to better resolve localized features such as discontinuities or abrupt variations in displacement magnitude. Additionally, the multigrid scheme improves the conditioning of the operator learning problem by accelerating the propagation of low-frequency information across the domain, reducing the burden on deep layers to carry global context. The resulting balance between long-range coherence and local precision is reflected in the lower error metrics relative to baseline architectures. In addition to accuracy, MG-FNO shows markedly higher throughput (8.08 it/s), suggesting its multiscale computations are amenable to efficient implementation. These findings suggest that incorporating explicit multiscale structure not only improves

predictive accuracy but also enhances physical fidelity in regions of clinical or biomechanical importance, where displacement gradients carry critical diagnostic information.

4.2 DeepONet Evaluation

The DeepONet demonstrated mixed performance across the real and imaginary displacement fields, with results that were generally less competitive than the FNO-based models in terms of accuracy, but superior in terms of computational efficiency. For the real displacement fields, DeepONet achieved an MSE of 0.0064, MAE of 0.0567, RMSE of 0.0801, and an accuracy of 0.8349. These values indicate that while the model successfully captured the correct magnitude range of displacements, it exhibited a consistent smoothing bias in its predictions. Visual inspection confirmed that DeepONet outputs lacked the fine-scale spatial variability observed in the ground truth, leading to underrepresentation of localized gradients and biomechanical heterogeneity that are critical for modeling traumatic brain injury, as displayed in Figure 7b. This smoothing effect suggests that although the architecture is effective at learning global trends, its branch–trunk structure does not adequately represent the high-frequency components of the displacement field. Consequently, DeepONet underperformed relative to FNO, F-FNO, and MG-FNO, all of which better recovered localized displacement variations.

By contrast, for the imaginary displacement fields, DeepONet achieved substantially stronger performance, with an MSE of 0.0028, MAE of 0.0429, RMSE of 0.0532, and accuracy of 0.9400. Notably, this MSE outperformed even the MG-FNO (0.0045) and F-FNO (0.0101), making DeepONet the most accurate model for this component. The imaginary fields feature smoother global variations relative to the real component, which reduces the reliance on resolving high-frequency content. Under these conditions, DeepONet’s global functional representation aligns more closely with the data structure, highlighting a strong dependence of DeepONet’s effectiveness on the spectral content of the target field. From a computational standpoint, DeepONet was the most efficient architecture tested, achieving 14.54 iterations per second with only 2.1M trainable parameters (Table 2). This represents nearly a $7.3\times$ speedup relative to MG-FNO and an order of magnitude fewer parameters than all FNO-based variants. These properties underscore its potential for lightweight deployment in real-time applications, provided that the loss of spatial fidelity in complex, high-gradient fields can be addressed.

5 Conclusions

This study provides the first systematic benchmark of neural operator architectures for patient-specific modeling of traumatic brain injury (TBI) biomechanics. By leveraging a multimodal dataset of magnetic resonance elastography (MRE) displacement fields, we demonstrate that Fourier Neural Operator (FNO)-based models and Deep Operator Networks (DeepONet) can accurately predict full-field brain deformation across physiologically relevant frequency ranges while reducing computation time from hours to milliseconds. Among the tested architectures, the Multi-Grid FNO (MG-FNO) achieved the highest accuracy (94.3% spatial fidelity), particularly in capturing fine-scale, high-gradient displacement patterns critical for injury assessment. Factorized FNO (F-FNO) achieved the fastest training convergence, whereas DeepONet delivered the most efficient inference, suggesting potential for lightweight, real-time deployment on edge devices.

These findings represent a paradigm shift for computational neurobiomechanics. Neural operator-based surrogates bridge the gap between high-fidelity finite element models and the speed required for clinical translation, enabling **real-time digital twins** of the human brain. Such models could transform how TBI is managed by supporting rapid triage decisions in emergency settings, sideline concussion evaluation in sports, and personalized helmet or protective equipment design. In research and public health contexts, scalable operator-based models may facilitate population-level simulations to identify vulnerable subgroups and inform injury prevention policies.

Despite these advances, several challenges remain. The models exhibited residual spectral bias, underpredicting localized, high-frequency deformation modes most relevant to tissue-level injury risk. Future work should focus on incorporating multiscale frequency learning, hybrid physics-informed loss functions, and uncertainty quantification to improve robustness and interpretability. Extending these models to time-resolved, nonlinear impact scenarios and validating them on independent, multi-site datasets will be essential for clinical translation.

In conclusion, neural operators hold significant promise as clinically deployable tools for rapid, individualized prediction of brain biomechanics. By uniting subject-specific imaging, operator learning, and high-throughput inference, this work lays the groundwork for precision neurotrauma modeling—shifting computational biomechanics from retrospective research analyses toward proactive, real-time clinical decision support.

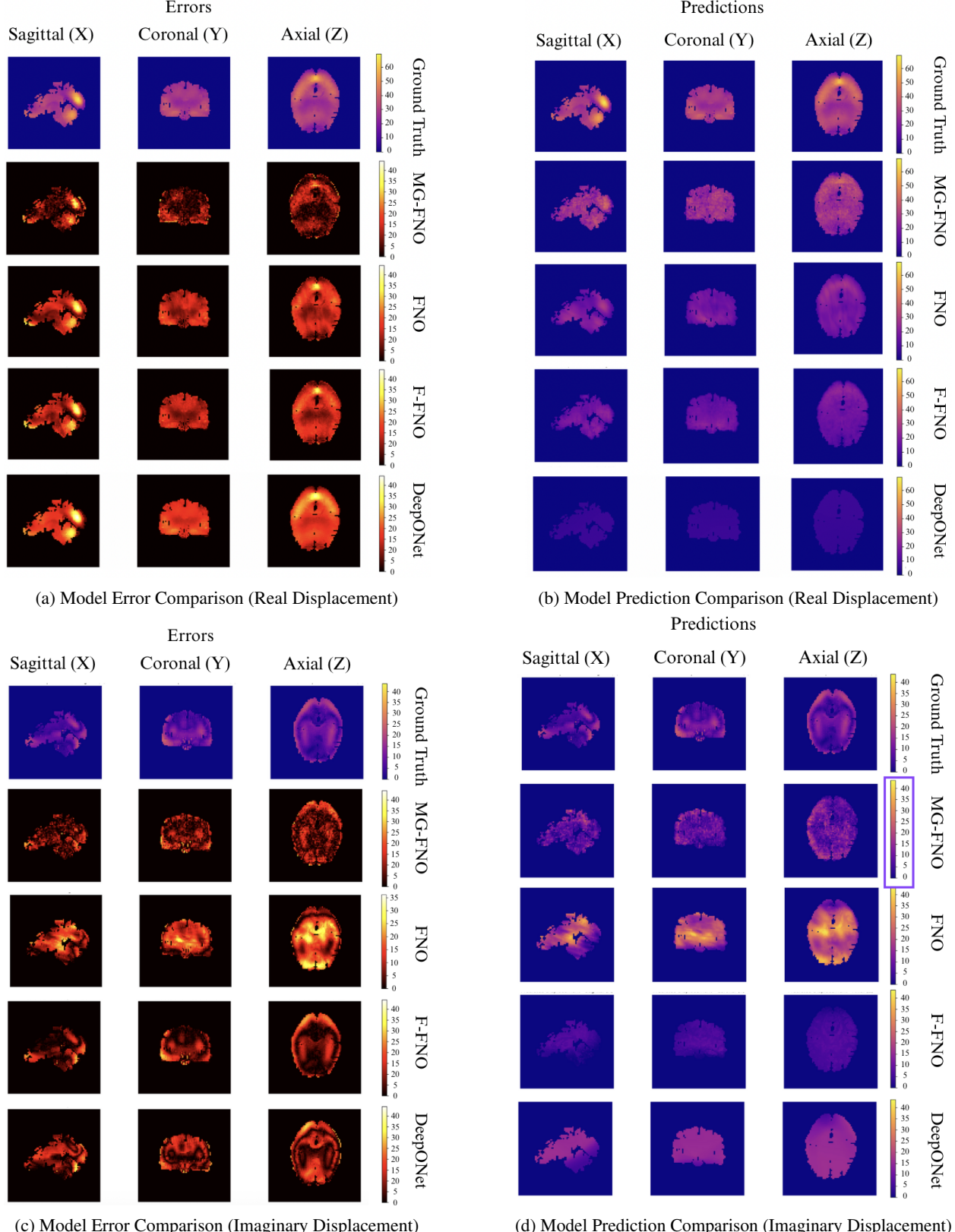


Figure 7: Comparison of Model Errors and Predictions across Real and Imaginary Displacement Fields. The FNO and F-FNO predict quite similarly on the real displacement fields, with a spectral bias issue evident. The MG-FNO struggles less with this issue, and has the strongest real displacement performance. The DeepONet model has less of a spectral bias here, but struggles with capturing local transitions.

6 Acknowledgments

The authors would like to acknowledge computing support provided by the Advanced Research Computing at Hopkins (ARCH) core facility at Johns Hopkins University and the Rockfish cluster. ARCH core facility (`rockfish.jhu.edu`) is supported by the National Science Foundation (NSF) grant number OAC1920103. The authors gratefully acknowledges the Brain Biomechanics Imaging Repository (<http://www.nitrc.org/projects/bbir>) for data which was supported under grants U01 NS112120 and R56 NS055951. The research efforts of DRS and SG are supported by National Science Foundation (NSF) under Grant No. 2436738. Any opinions, findings, conclusions, or recommendations expressed in this material are those of the author(s) and do not necessarily reflect the views of the funding organizations.

Author contributions

Conceptualization: AA, DRS, SG
 Investigation: AA, DRS, SG
 Visualization: AA, DRS, SG
 Supervision: SG
 Writing - original draft: AA, DRS
 Writing - review & editing: AA, DRS, SG

Data and code availability

The data is publicly available on <http://www.nitrc.org/projects/bbir>. The neural operator codes that support the findings of this study are available on <https://github.com/Centrum-IntelliPhysics/Neural-Operator-for-Traumatic-Brain-Injury>.

Competing interests

The authors declare no competing interest

References

- [1] Centers for Disease Control and Prevention. TBI Data | Traumatic Brain Injury and Concussion. <https://www.cdc.gov/traumatic-brain-injury/data-research/index.html>, 2024. Published October 29, 2024. Accessed September 20, 2025.
- [2] Chanel Matney, Katherine Bowman, and Donald Berwick. Traumatic Brain Injury: A Roadmap for Accelerating Progress. 2022.
- [3] L. Hu, S. Yang, B. Jin, and C. Wang. Advanced neuroimaging role in traumatic brain injury: A narrative review. *Frontiers in Neuroscience*, 16:872609, 2022.
- [4] H. Bahreinizad, S. K. Chowdhury, G. Paulon, L. Wei, and F. Z. Santos. Development and validation of an mri-derived head-neck finite element model. *bioRxiv*, 2023.
- [5] A. D. Gomez, A. K. Knutsen, F. Xing, Y. C. Lu, D. Chan, D. L. Pham, P. V. Bayly, and J. L. Prince. 3-d measurements of acceleration-induced brain deformation via harmonic phase analysis and finite-element models. *IEEE Transactions on Biomedical Engineering*, 66(5):1456–1467, 2019.
- [6] E. Griffiths and S. Budday. Finite element modeling of traumatic brain injury: Areas of future interest. *Current Opinion in Biomedical Engineering*, 24:100421, 2022.
- [7] S. Wu, W. Zhao, and S. Ji. Real-time dynamic simulation for highly accurate spatiotemporal brain deformation from impact. *Computer Methods in Applied Mechanics and Engineering*, 394:114913, 2022.
- [8] L. Lu, P. Jin, and G. E. Karniadakis. Deeponet: Learning nonlinear operators for identifying differential equations based on the universal approximation theorem of operators, 2019.
- [9] Z. Li, N. Kovachki, K. Azizzadenesheli, B. Liu, K. Bhattacharya, A. Stuart, and A. Anandkumar. Fourier neural operator for parametric partial differential equations, 2021.

[10] P. V. Bayly, K. Cohen, T. Leister, E. Alshareef, S. C. Benson, K. D. Miller, and T. J. Bruns. Mr imaging of human brain mechanics in vivo: New measurements to facilitate the development of computational models of brain injury. *Annals of Biomedical Engineering*, 49:2677–2692, 2021.

[11] T. Chen and H. Chen. Universal approximation to nonlinear operators by neural networks with application to dynamical systems. *IEEE Transactions on Neural Networks*, 6(4):911–917, 1995.

[12] Alasdair Tran, Alexander Mathews, Lexing Xie, and Cheng Soon Ong. Factorized fourier neural operators. In *International Conference on Learning Representations (ICLR)*, pages 417–422. IEEE, 2023.

[13] Jean Kossaifi, Nikola Kovachki, Kamyar Azizzadenesheli, and Anima Anandkumar. Multi-grid tensorized fourier neural operator for high-resolution pdes, 2023.

[14] Somdatta Goswami, Katiana Kontolati, Michael D Shields, and George Em Karniadakis. Deep transfer operator learning for partial differential equations under conditional shift. *Nature Machine Intelligence*, 4(12):1155–1164, 2022.

[15] Vijay Kag, Dibakar Roy Sarkar, Birupaksha Pal, and Somdatta Goswami. Learning hidden physics and system parameters with deep operator networks. *arXiv preprint arXiv:2412.05133*, 2024.

[16] Somdatta Goswami, Dimitris G Giovanis, Bowei Li, Seymour MJ Spence, and Michael D Shields. Neural operators for stochastic modeling of nonlinear structural system response to natural hazards. *arXiv preprint arXiv:2502.11279*, 2025.

[17] Thorsten Kurth, Shashank Subramanian, Peter Harrington, Jaideep Pathak, Morteza Mardani, David Hall, Andrea Miele, Karthik Kashinath, and Anima Anandkumar. Fourcastnet: Accelerating global high-resolution weather forecasting using adaptive fourier neural operators. In *Proceedings of the platform for advanced scientific computing conference*, pages 1–11, 2023.

[18] Somdatta Goswami, Aniruddha Bora, Yue Yu, and George Em Karniadakis. Physics-informed deep neural operator networks. In *Machine learning in modeling and simulation: methods and applications*, pages 219–254. Springer, 2023.

[19] Andreas Maier, Harald Köstler, Marco Heisig, Patrick Krauss, and Seung Hee Yang. Known operator learning and hybrid machine learning in medical imaging—a review of the past, the present, and the future. *Progress in Biomedical Engineering*, 4(2):022002, 2022.

[20] Qianying Cao, Somdatta Goswami, and George Em Karniadakis. Laplace neural operator for solving differential equations. *Nature Machine Intelligence*, 6(6):631–640, 2024.

[21] Katiana Kontolati, Somdatta Goswami, George Em Karniadakis, and Michael D Shields. Learning nonlinear operators in latent spaces for real-time predictions of complex dynamics in physical systems. *Nature Communications*, 15(1):5101, 2024.

[22] Sharmila Karumuri, Lori Graham-Brady, and Somdatta Goswami. Physics-informed latent neural operator for real-time predictions of complex physical systems. *arXiv preprint arXiv:2501.08428*, 2025.

[23] Wei Wang, Maryam Hakimzadeh, Haihui Ruan, and Somdatta Goswami. Time-marching neural operator–fe coupling: Ai-accelerated physics modeling. *Computer Methods in Applied Mechanics and Engineering*, 446:118319, 2025.

[24] Dibakar Roy Sarkar, Chandrasekhar Annavarapu, and Pratanu Roy. Adaptive interface-pinns (adai-pinns) for inverse problems: Determining material properties for heterogeneous systems. *Finite Elements in Analysis and Design*, 249:104373, 2025.

[25] Dibakar Roy Sarkar, Chandrasekhar Annavarapu, and Pratanu Roy. Interface physics-informed neural networks (i-pinns) to solve inverse problems in heterogeneous materials. 2025.

[26] Dibyajyoti Nayak and Somdatta Goswami. Ti-deepnet: Learnable time integration for stable long-term extrapolation. *arXiv preprint arXiv:2505.17341*, 2025.

[27] Luis Mandl, Dibyajyoti Nayak, Tim Ricken, and Somdatta Goswami. Physics-informed time-integrated deepnet: Temporal tangent space operator learning for high-accuracy inference. *arXiv preprint arXiv:2508.05190*, 2025.

[28] Bahador Bahmani, Somdatta Goswami, Ioannis G Kevrekidis, and Michael D Shields. A resolution independent neural operator. *Computer Methods in Applied Mechanics and Engineering*, 444:118113, 2025.

[29] Luis Mandl, Somdatta Goswami, Lena Lambers, and Tim Ricken. Separable physics-informed deepnet: Breaking the curse of dimensionality in physics-informed machine learning. *Computer Methods in Applied Mechanics and Engineering*, 434:117586, 2025.

[30] Varun Kumar, Somdatta Goswami, Katiana Kontolati, Michael D Shields, and George Em Karniadakis. Synergistic learning with multi-task deepnet for efficient pde problem solving. *Neural Networks*, 184:107113, 2025.

- [31] A. Paszke, S. Gross, F. Massa, A. Lerer, J. Bradbury, G. Chanan, T. Killeen, Z. Lin, N. Gimelshein, L. Antiga, A. Desmaison, A. Köpf, E. Yang, Z. DeVito, M. Raison, A. Tejani, S. Chilamkurthy, B. Steiner, L. Fang, J. Bai, and S. Chintala. Pytorch: An imperative style, high-performance deep learning library, 2019.
- [32] D. Hendrycks and K. Gimpel. Gaussian error linear units (gelus), 2016.
- [33] I. Loshchilov and F. Hutter. Decoupled weight decay regularization, 2017.